Geocarto International

ISSN: (Print) (Online) Journal homepage: https://www.tandfonline.com/loi/tgei20

Assessing the impacts of human interventions and climate change on fluvial flooding using CMIP6 data and GIS-based hydrologic and hydraulic models

Purushottam Kumar Mahato, Dharmaveer Singh, Birendra Bharati, Alexandre S. Gagnon, Bhupendra Bahadur Singh & Javanarayanan Brema

To cite this article: Purushottam Kumar Mahato, Dharmaveer Singh, Birendra Bharati, Alexandre S. Gagnon, Bhupendra Bahadur Singh & Javanarayanan Brema (2022): Assessing the impacts of human interventions and climate change on fluvial flooding using CMIP6 data and GIS-based hydrologic and hydraulic models, Geocarto International, DOI: 10.1080/10106049.2022.2060311

To link to this article: https://doi.org/10.1080/10106049.2022.2060311

Published online: 11 Apr 2022.

GEOCARTO INTERNATIONAL
https://doi.org/10.1080/10106049.2022.2060311

Taylor & Francis
Taylor & Francis Group

Assessing the impacts of human interventions and climate change on fluvial flooding using CMIP6 data and GIS-based hydrologic and hydraulic models

Purushottam Kumar Mahato[a], Dharmaveer Singh[b], Birendra Bharati[a], Alexandre S. Gagnon[c], Bhupendra Bahadur Singh[d] and Javanarayanan Brema[e]

[a]Department of Water Engineering & Management, Central University of Jharkhand, Ranchi, India; [b]Symbiosis Institute of Geoinformatics, Symbiosis International (Deemed University), Pune, India; [c]School of Biological and Environmental Sciences, Liverpool John Moores University, Liverpool, UK; [d]Indian Institute of Tropical Meteorology (Ministry of Earth Sciences), Centre for Climate Change Research, Pune, India; [e]Department of Civil Engineering, Karunya Institute of Technology and Sciences (Deemed-to-be-University), Coimbatore, India

ABSTRACT

This study presents an approach for modelling and mapping fluvial flooding, considering both land use/land cover (LULC) change and climate change, and applies it to the Brahmani River Basin in eastern India. Climate change projections were obtained from the Coupled Model Intercomparison Project Phase 6 (CMIP6), and their impacts on the hydrology of the catchment were investigated using HEC-HMS and HEC-RAS software. Results reveal that changes in LULC types, specifically an increase in proportions of agricultural and built-up areas and a decrease in forest cover, as undergone between years 1985 and 2018, have increased peak discharge following a storm, thereby causing an increase in spatial extent of floods of different return periods. Moreover, downscaled climate change scenarios from two General Circulation Models were used to determine potential changes in river discharge according to two GHG emission scenarios from the latest IPCC: SSP245 and SSP585. The projections indicate that peak discharge and the spatial extent of flooded areas will increase for floods with return periods ranging from two to 100 years. This study demonstrates the important influence that changes in LULC have had on the susceptibility of the BRB to flooding, with climate change projected to further enhance the risk of flooding as the century progresses.

ARTICLE HISTORY
Received 28 June 2021
Accepted 27 March 2022

KEYWORDS
Fluvial flooding; land use/land cover; GIS-based hydrologic and hydraulic models; climate change; Brahmani River Basin

1. Introduction

Extreme weather and climate-related disasters, for instance, storms, landslides, heatwaves, droughts, and flooding, including glacier lake outbursts, affect many countries worldwide

CONTACT Dharmaveer Singh veermnnit@gmail.com; Alexandre S. Gagnon A.Gagnon@ljmu.ac.uk
This article has been corrected with minor changes. These changes do not impact the academic content of the article.

(Wallemacq et al. 1995; Quirós and Gagnon 2020). Nonetheless, of all natural hazards, flooding is the most recurrent and widespread disaster (Merz et al. 2007; Gómez-Palacios et al. 2017; Jain et al. 2019; Shafapour Tehrany et al. 2019). During the period 1995–2015, for instance, flooding accounted for nearly half of all weather-related disasters worldwide (Wallemacq et al. 2018) and it has been reported to be responsible for as many as a third of all deaths, injuries and damages caused by natural disasters (Sanyal and Lu 2004). India is one of the countries most affected by floods (Dhar and Nandargi 2003; Jain et al. 2019); they affect many regions of the country every year, with most episodes being the result of excessive rainfall during the Southwest monsoon season, which extends from June through September (Dhar and Nandargi 2003). According to EM-DAT (2020), there were 353 floods reported across the country from 1926 to 2020, causing approximately 80,000 deaths, in addition to damages estimated at approximately $US 7.3 billion.

Hu et al. (2018) reported an increase in the occurrence of floods across the globe and inevitably in the number of people affected by floods during the period 1975–2016, a trend that they associated with human interventions on the landscape and climate change (Kjeldsen 2010; Zope et al. 2016; Dang and Kumar 2017). Worldwide, the two main human interventions that have altered the LULC of many catchments are urbanisation and the conversion of natural ecosystems to agriculture (Ramankutty and Foley 1999; Veach et al. 2017). Changes in LULC types can affect the speed of the flow of water following a storm on the ground surface as well as the natural course of rivers and, consequently, the risk of flooding. The latter is particularly the case for rivers that have had their conveyance capacity reduced as a result of an increase in bedload sediment transport and the ensuing morphological changes (Pramanik et al. 2010; Singh and Awasthi 2011; Miller and Hutchins 2017). Wan and Yang (2007), for instance, found that an increase in the proportion of build-up areas in the catchment of Taihu Lake in China was one of the primary factors for higher flood risk, with similar conclusions also reached by Shi et al. (2007) in another catchment in China and Saghafian et al. (2008) in Iran. Bosch and Hewlett (1982), for its part, found a high correlation between deforestation and recent changes in the frequency and intensity of floods in small catchments, a correlation which other studies focusing on larger catchments had not identified (e.g. Beschta et al. 2000; Andréassian 2004). In addition, climate change is a factor often suggested for the increasing trend in the severity of floods in many parts of the world (Frey et al. 2010; Zhai et al. 2018), given the projected intensification of the hydrological cycle under climate change (Déry et al. 2009; Wu et al. 2013). A warmer atmosphere can store more moisture and therefore extreme precipitation events are more likely (Singh et al. 2021), increasing the potential for flash-flooding (Schiermeier 2011; Alfieri et al. 2015).

Reducing vulnerability and building resilience to flooding requires the implementation of a comprehensive, practical and integrated flood management strategy (Merwade et al. 2008; Wilby and Keenan 2012), which generally involves the identification of zones at risk of flooding on the basis of flood monitoring and modelling, the construction of physical infrastructure (e.g. dams, embankments, levees and spurs on the river banks) to protect against floods, planning and regulation of land use, and the development of flood early warning systems. Amongst all measures, the modelling of floods to generate flood risk maps is considered the most efficient approach (Merwade et al. 2008; Shafapour Tehrany et al. 2019), with other measures usually developed and implemented on the basis of those maps.

With the scientific and technological advancements in distributed hydrological and hydraulic models, as well as the availability of climate change scenarios downscaled to the scale of river catchments, our ability to simulate and predict the magnitude and frequency of future flood events has improved significantly in recent years (Knebl et al. 2005; Forte

et al. 2006; Pradhan 2010). The availability of high-resolution remote sensing data, which are used to develop Digital Elevation Models (DEMs) and to provide estimates of rainfall and evapotranspiration at an appropriate spatiotemporal resolution, and to identify soil and LULC types over catchments has further improved the accuracy of these predictions (Brivio et al. 2002; Patro et al. 2009; Zope et al. 2016; Quirós and Gagnon 2020).

Hydrological models such as the Hydrologic Modelling System from the Hydrologic Engineering Centre (HEC-HMS) are commonly used to investigate potential changes in river discharge under climate change and/or as a result of changes in LULC (Knebl et al. 2005; Sanyal et al. 2014; Hu and Shrestha 2020). Hydraulic or hydrodynamic models, for their part, such as the River Analysis System of the Hydrologic Engineering Centre (HEC-RAS) are by and large utilised to simulate the spatial extent and depth of floods (Mokhtar et al. 2018). For this reason, several studies have used either the HEC-HMS or the HEC-RAS models, or an integration of the two models, to simulate flood peaks, and to estimate the spatial extent of floods. Sanyal et al. (2014), for instance, analysed the impact of changes in LULC on the runoff of the Konar River in eastern India using HEC-HMS, while Mokhtar et al. (2018) developed a flood inundation map on the basis of a given discharge for the Padang Terap River in Malaysia using HEC-RAS, while integrating the two models has provided reliable results in fluvial flood studies, for instance, Knebl et al. (2005) in Texas and Abdessamed and Abderrazak (2019) in the arid environments of southwestern Algeria. In India, Zope et al. (2016) integrated the HEC-HMS model with the HEC-RAS software to assess impacts of changes in LULC on flooding between 1966 and 2009 in the Oshiwara river catchment in Mumbai, which has experienced an expansion of urban areas into flood plains.

The Brahmani River Basin (BRB) is an important basin in India, but it is recurrently affected by flooding (Pramanik et al. 2010; Rai et al. 2018). A number of studies have previously been conducted to model floods of various return periods over the basin, with the purpose of delineating areas at risk of flooding. Pramanik et al. (2010) studied the efficacy of a Digital Elevation Model (DEM) over the Brahmani River catchment to simulate the magnitude of a flood. Rai et al. (2018) developed a coupled hydrological-hydrodynamic model to delineate the extent of inundation during floods in the deltas of the Brahmani and Baitarani rivers, while Sindhu and Durga Rao (2017) used the HEC-HMS and HEC-RAS models to forecast streamflow ahead of a flood and to simulate its potential inundation impact. These previous flood modelling studies over the BRB neither did investigate the effects of changes in LULC types on flood risk nor the potential impacts of climate change. The latter is important given that a number of studies have suggested that the BRB is likely to experience severe flooding under climate change (Dahm et al. 2019; Vandana et al. 2019; Bharat and Mishra 2021). Moreover, better knowledge of the impacts of changes in LULC, notably as a result of the rapid urbanisation that the basin has experienced in recent decades, is vital for the development of effective strategies to prevent and mitigate the risk of flooding (Bharat and Mishra 2021).

This study examines the impacts of anthropogenic interventions and future climate change on flood peaks, and then generates flood risk maps for floods of various return periods over the BRB. For this purpose, it considers the changes in LULC type that the basin has experienced in recent decades and climate change projections by simulating floods of a 2-year, 10-year, 25-year, 50-year and 100-year return periods using the HEC-HMS and HEC-RAS models.

2. Study area

The BRB is an important river basin in India (Figure 1), supporting the livelihoods of 8.5 million people. Upstream of the Brahmani River is the South Koel River, which originates

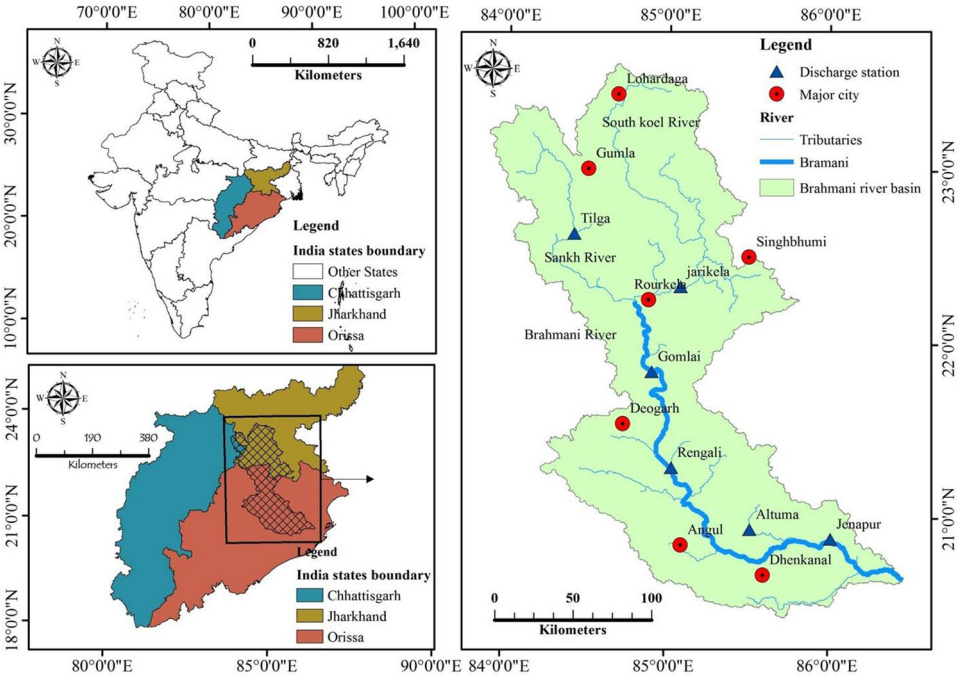

Figure 1. Map of the BRB, its location in India, and the location of the river discharge stations over the basin.

in Jharkhand State (CPSP Report 2015). The South Koel River joins the Sankh River in Orissa State where the combined flow of both rivers is then known as the Brahmani River. The Brahmani River runs through Orissa State prior to flow into the Bay of Bengal. During the course of its flow, the river is joined by numerous tributaries, which enhance the influx of water during the monsoon season, occasionally causing the riverflow to be turbulent during that season. On an annual basis, the daily maximum, minimum and mean flow of the Brahmani River during the period 2000–2014 was 10,372 m^3/s, 23.5 m^3/s and 512.3 m^3/s, respectively, at Jenapur.

The surface area of the BRB was estimated at 39,045 km^2, of which 57.3% lies in Orissa, 40.4% in Jharkhand and 2.3% in the State of Chhattisgarh, by delineating the catchment using the Terra Advanced Spaceborne Thermal Emission and Reflection Radiometer (ASTER) Global DEM (GDEM).[1] It is the second largest river basin in Orissa State. The BRB is characterised by a humid and sub-tropical climate. According to the India Meteorological Department (IMD) gridded dataset, total annual precipitation was 1388.8 mm during the period 1981–2018 over the catchment, with the majority of which (~80%) falling during the summer monsoon season. The catchment experiences strong inter-annual variability in total annual precipitation, with the lowest (971.3 mm) and highest (1755 mm) amounts of precipitation recorded in 2010 and 1994, respectively during the above period.

The BRB is abundant in terms of water resources. The water resource potential of the basin is estimated at 2.1×10^{10} m^3/year (CPSP Report 2015). In addition to meeting the domestic and industrial demand for water, water is used for irrigation. Agriculture is intensive in the deltaic part of the basin, and irrigation is provided through the Rengali dam project. The reservoir formed by the dam covers a surface area of 25,250 km^2 and has a water storage capacity of 3.4×10^9 m^3. The dam was constructed in 1985 with the primary purpose of protecting the population living in the delta from flooding,

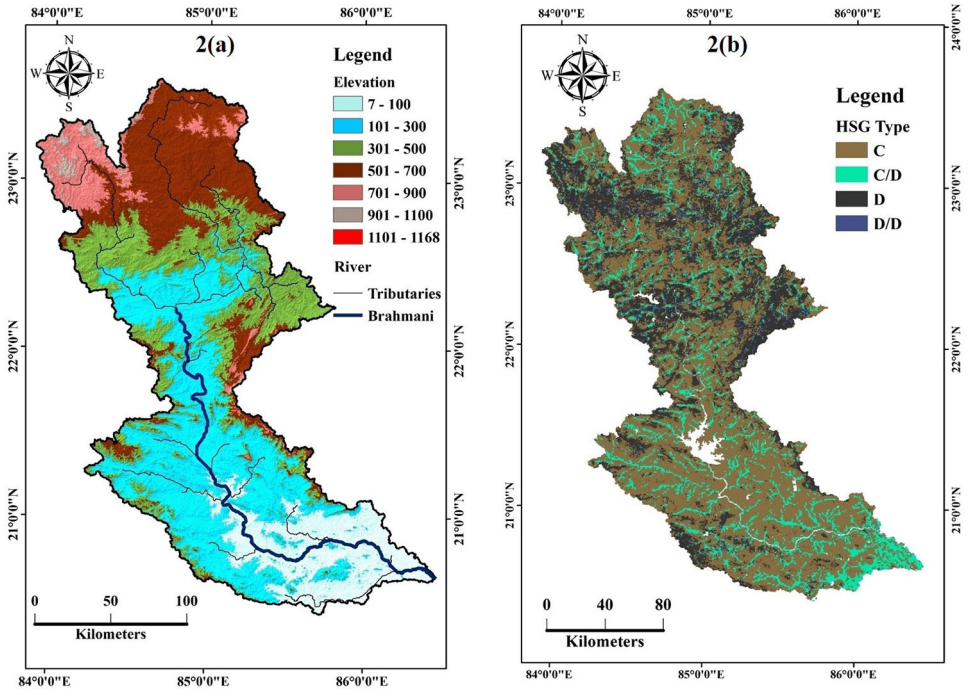

Figure 2. Variation in elevation (a) and soil types (b) over the BRB.

particularly the devastating floods of August 1975, which affected millions of peoples and caused huge economic losses (Maske and Day 1975). Although Rengali dam has significantly reduced the risk of high floods, the BRB is recurrently affected by floods, with floods occurring every few years (Rai et al. 2018), and with increasing economic losses.[2]

The regional hydrology of the BRB has changed considerably in recent decades, not only due to changes in LULC, but also because of climate change (Islam et al. 2012). Observations show that eastern India, including the BRB, has become warmer during the period 1986–2015 (Krishnan et al. 2020), and that temperature will continue to increase in the near and far future, according to the ensemble mean of the South Asia multi-Regional Climate Model (RCM) of the World Climate Research Programme (WCRP) Coordinated Regional Climate Downscaling Experiment (CORDEX) (Sanjay et al. 2020a, 2020b). Furthermore, the region has experienced an increasing, albeit weak, trend in total annual rainfall, but this increase is projected to become more significant as the climate continues to warm (Krishnan et al. 2020). An increase in average precipitation will further increase the probability of extreme precipitation events, with the latter having the potential to increase peak flow and thus the risk of flooding.

3. Data

3.1. Hydro-meteorological data

Daily discharge data for the Brahmani River were obtained from the India Water Resources Information System (WRIS)[3] for four stations as detailed in Table 1 and depicted in Figure 1. Daily temperature and rainfall data, available at a resolution of

0.25°×0.25°, were obtained from IMD for the period 1981–2018, with the catchment area represent by 59 grid cells in the dataset.

3.2. Topographical data

Topographical information is important in hydrological studies, as it controls the rainfall-runoff response over a basin (Horritt and Bates 2002). Such information is typically obtained from a DEM, which can be generated using surveying, the digitisation of existing topographic or contour maps, photogrammetry and remote sensing (Hawker et al. 2018), with most DEMs nowadays generated using remote sensing (Smith and Clark 2005). This study uses a DEM with 30 m resolution, which was downloaded from ASTER GDEM[4] (Figure 2a). Data from ASTER GDEM version 3 is freely available and covers the entire globe between 83°N and 83° S. The DEM data was used to delineate the basin and to generate Triangulated Irregular Network (TIN), which were then used to extract various topographical and hydrological parameters that were required as inputs into the hydrological and hydraulic models described below.

3.3. Satellite data

Information on the LULC types covering a river catchment is an integral part of a hydrological modelling study, because it is used to determine Manning's roughness coefficient and the runoff curve number (CN). Multi-spectral satellite data from Landsat-4 (spatial resolution: 56 m), Landsat-5 (spatial resolution: 30 m) and Sentinel-2A (spatial resolution: 10/20 m), which were acquired from the United States Geological Survey (USGS) Earth Explorer website[5] were used to prepare the LULC maps of the basin for the year 1985, 2005 and 2018 (Table 2). Manning's roughness coefficients for each LULC were obtained from Chow et al. (1988).

3.4. Soil data

Data on the Hydrological Soil Groups (HSGs) of the basin were downloaded from the Oak Ridge National Laboratory (ORNL) based Distributed Active Archive Centre (DAAC)[6] at a 250 m resolution. In this dataset, the soils are grouped into four major categories depending on their infiltrability and thus runoff potential (Ross et al. 2018). Figure 2b illustrates the soil classification map over the BRB, as used in this study. It can be seen that most of the basin is covered by soils falling into category C and D, which are characterised as having a loamy and clayey soil structures with a relatively low infiltration rate and thus high runoff potential.

3.5. Climate change scenarios

General (also referred to as Global) Circulation Models (GCMs) are used to determine how the climate might evolve in the future, typically up to the year 2100, under different scenarios of emissions of greenhouse gases (GHGs) into the atmosphere. Given their computational requirements, the outputs from GCMs are provided at a coarse spatial resolution of approximately 1.0°×1.0° and, for this reason, they cannot readily be used in impact studies focusing at the regional scale (Singh et al. 2015a), where the need for projections at a higher spatial resolution is often required, notably in regions of complexed topography (Singh et al. 2015b).

Table 2. Information on the satellite data used to prepare the LULC maps over the BRB.

Satellite system	Sensor	Path/row/or Tile number	Bands (μm)	Spatial resolution	Dates of acquisition
Landsat-4	Thematic Mapper (TM)	139/45	Band 1 (0.45–0.52)	56m	21-04-1985
		140/44	Band 2 (0.52–0.60)		28-04-1985
		140/45	Band 3 (0.63–0.69)		28-04-1985
		140/46	Band 4 (0.69–0.76)		28-04-1985
		141/43	Band 5 (1.55–1.75)		19-04-1985
		141/44	Band 7 (2.08–2.35)		19-04-1985
		141/45			19-04-1985
		141/46			19-04-1985
		142/44			26-04-1985
Landsat-5	Thematic Mapper (TM)	141/46	Band 1 (0.45–0.52)	30m	02-04-2005
		141/45	Band 2 (0.52–0.60)		02-04-2005
		141/44	Band 3 (0.63–0.69)		02-04-2005
		139/46	Band 4 (0.69–0.76)		04-04-2005
		139/45	Band 5 (1.55–1.75)		20-04-2005
		140/45	Band 7 (2.08–2.35)		27-04-2005
		140/46			27-04-2005
		140/44			27-04-2005
Sentinel-2A	Multi-spectral Imager (MSI)	T44QQL	Band 2 (0.490)	10/20m	21-04-2018
		T44QQM	Band 3 (0.560)		11-05-2018
		T44QRM	Band 4 (0.665)		08-05-2018
		T44QRL	Band 5 (0.705)		21-04-2018
		T45QTC	Band 6 (0.740)		18-05-2018
		T45QTD	Band 7 (0.783)		18-04-2018
		T45QTE	Band 8 (0.842)		08-05-2018
		T45QTF	Band 8A (0.865)		18-05-2018
		T45QTG			18-05-2018
		T45QUC			18-05-2018
		T45QUD			18-05-2018
		T45QUE			08-05-2018
		T45QUF			08-05-2018
		T45QUG			08-05-2018
		T45QVC			18-05-2018
		T45QVD			18-05-2018

An investigation of the potential changes in runoff over the BRB requires projections of future changes in precipitation and evapotranspiration, with the latter often estimated using temperature projections. Accordingly, temperature and precipitation projections were obtained from Mishra et al. (2020), a dataset providing bias corrected and downscaled GCM outputs for river basins across South Asia[7] from 13 models taking part of the Coupled Model Intercomparison Project Phase 6 (CMIP6). Climate change projections are available for the historical (1951–2014) and future (2015–2100) time-periods for the four latest GHG emission scenarios from the Intergovernmental Panel on Climate Change (IPCC): Shared Socioeconomic Pathways (SSP) 126, 245, 370 and 585. The projections are available at a daily time-scale and at a spatial resolution of $0.25^{\circ} \times 0.25^{\circ}$. Out of available models, outputs from the two models that best capture the variability of temperature and rainfall over South Asia were obtained, namely Earth Consortium (EC)-Earth 3 and the Meteorological Research Institute Earth System Model version 2 (MRI-ESM2) for the last 30-year period of this century, i.e. 2071–2100, hereafter referred to as the 2080s, and for the SSP245 and SSP585 GHG emission scenarios. The latter were chosen so as to assess the uncertainty in the scenarios in terms of future GHG emission; SSP585 provides the most severe emission of GHGs into the 21st century, while SSP126 is the most optimistic, although it is already too late for this scenario to materialised in view of past emissions, and for this reason, the most optimistic scenario used in this study was SSP245.

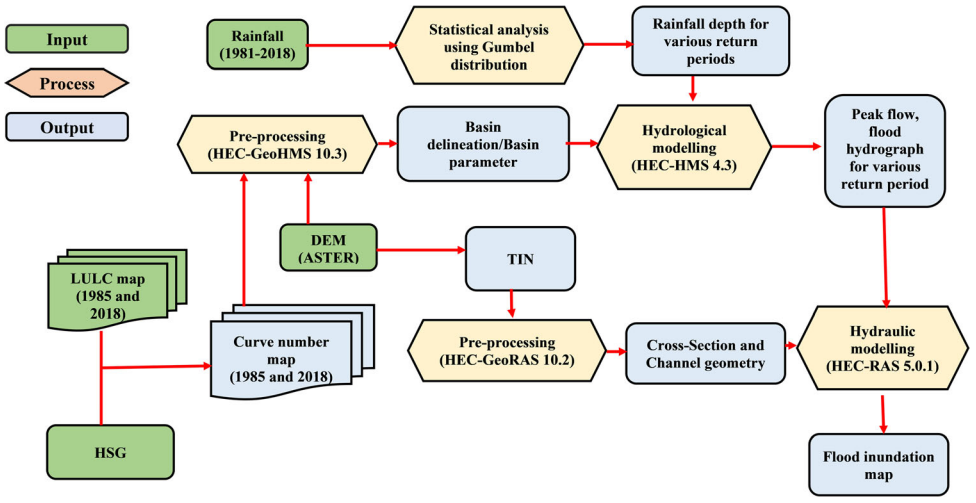

Figure 3. Methodology showing major steps involved in the peak flow and flood hydrograph generation from HEC-HMS and the integration of HEC-HMS with HEC-RAS model for modelling flood inundated areas in the BRB.

4. Methods

Figure 3 systematically explains the methodology adopted in this study. The models used, and steps involved in flood inundation modelling were discussed under the following sub-sections:

4.1. Hydrological modelling using HEC-HMS

HEC-HMS, version 4.3, is a distributed hydrologic model developed by the U.S. Army Corps of Engineers at the Hydrologic Engineering Centre (HEC) (Feldman 2000; Knebl et al. 2005). The model was used to simulate the hydrological processes over the BRB catchment, including an estimation of peak flows. HEC-GeoHMS version 10.3, an extension of ArcGIS, was used for terrain processing and for estimating the model parameters such as basin, sub-basins, junctions, stream network and reaches from the DEM. CN values of sub-basins for 1985 LULC and 2018 LULC scenario were also calculated using 'Generate CN grid' tool available in HEC-GeoHMS. These were further used as inputs in HEC-HMS to setup the hydrological model for BRB. HEC-HMS has three main components: basin model manager, meteorological model manager and control specification manager. In this study hypothetical storm was selected to simulate the various return period of rainfall after calibration and validation. The duration of the event (simulation stat/end date and time) is controlled through the control specification manager. The topographical model-set up for the BRB is shown in Figure 4.

HEC-HMS includes different subroutines to estimate losses due to infiltration, which, in this study, were estimated using the SCS curve number (CN) method. It estimates runoff from a storm over any area based on LULC and hydrological soil groups using following equations (Knebl et al. 2005):

$$Q = \frac{(P - I_a)^2}{((P - I_a) + S)} \tag{1}$$

$$I_a = 0.2S \tag{2}$$

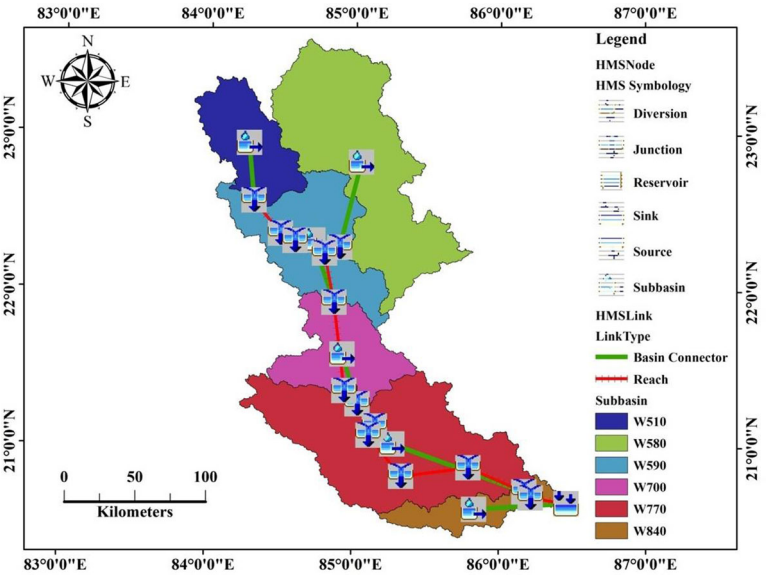

Figure 4. Established hydrological modelling setup for the BRB under HEC-HMS environment.

$$S = \frac{1000}{CN} - 10 \tag{3}$$

Substituting Eq. (2) into Eq. (1)

$$Q = \frac{(P - 0.2S)^2}{(P + 0.8S)} \tag{4}$$

where, Q is runoff, P is rainfall, S is potential maximum retention, I_a is initial abstraction and CN is the curve number.

The excess rainfall after infiltration is transformed into direct runoff using SCS unit hydrograph transform method at the outlet of sub-basin. The delay in time taken by water reaching at the outlet, i.e. Lag time (T_{lag}) and CN is required in SCS unit hydrograph method for transformation of excess rainfall into direct runoff (Subramanya 2008). T_{lag} is estimated as the equations given below (Hu and Shrestha 2020):

$$T_c = \frac{\left(L^{0.8} + (S+1)^{0.7}\right)}{(1900 + Y^{0.5})} \tag{5}$$

$$T_{lag} = T_c * 0.6 \tag{6}$$

where, T_c represents time of concentration, L is hydraulic length of the watershed and Y represents slope of the basin. Further, the peak unit hydrograph (U_p) is estimated from the equations given below (Feldman 2000):

$$U_P = 484 * \frac{A}{T_p} \tag{7}$$

$$T_P = \frac{\Delta t}{2} + T_{lag} \tag{8}$$

where, A refers to watershed area, T_p and Δt represents time of peak and excess rainfall duration, respectively. Initially, runoff for each sub-basin is computed using the

Muskingum routing method, which is later on collectively routed to the main basin outlet. It is based on storage-outflow relationship. Inflow, outflow, and storage for Muskingum routing are described as follows:

$$Q_{j+1} = C_1 I_{j+1} + C_2 I_J + C_3 Q_J \tag{9}$$

where, I_j and I_{j+1} are inflows at upstream at time j and $j+1$, respectively. Similarly, Q_j and Q_{j+1} are outflows at downstream at time j and $j+1$, respectively. $C1$, $C2$ and $C3$ are coefficient that can be estimated from the following equations:

$$C_1 = \frac{\Delta t - 2KX}{2K(1-X) + \Delta t} \tag{10}$$

$$C_2 = \frac{\Delta t + 2KX}{2K(1-X) + \Delta t} \tag{11}$$

$$C_3 = \frac{2K(1-X) - \Delta t}{2K(1-X) + \Delta t} \tag{12}$$

where, K is travel time of a flood wave passing through reach, X is a measure of the degree of storage, and Δt is time interval of simulation.

4.2. Model calibration and validation

The developed HEC-HMS model was calibrated and validated using discharge data from the Brahmani River at Gomlai in the upper reaches of the river and at Jenapur in its lower reaches. The calibration was performed in order to adjust model parameters so that the simulated flows have had better agreement with the observed flows. The daily discharge data of four years (2000–2004) was used in model calibration. The calibration process included a combination of software automated calibration and manual calibration methods. A comparison of simulated daily river flow with observed data was carried out for both calibration and validation period (Figure 5). Model performance was also evaluated using the Nash-Sutcliffe efficiency coefficient (*NSE*) and the coefficient of determination (R^2):

$$NSE = 1 - \left[\frac{\sum_{i=1}^{n} (O_i - P_i)^2}{\sum_{i=1}^{n} (O_i - O_{avg})^2} \right] \tag{13}$$

$$R^2 = \left[\frac{\sum_{i=1}^{n} (O_i - O_{avg})(P_i - P_{avg})}{\sum_{i=1}^{n} (O_i - O_{avg})^2 \sum_{i=1}^{n} (P_i - P_{avg})^2} \right]^2 \tag{14}$$

where, O_i is the i^{th} observed value, O_{avg} is the average observed value for the entire study period, P_i is the ith predicted (simulated) value, and P_{avg} is the average of the predicted value over the entire study period. The values of the *NSE* can range from $-\infty$ to 1 (Nash and Sutcliffe 1970), while those of R^2 vary from 0 to 1.

The simulated daily flow showed good agreement with the observed values at Jenapur for the calibration period with $NSE = 0.52$ and $R^2 = 0.58$. For the validation period, the simulated and observed daily flow also revealed good agreement as indicated by the values of *NSE* and R^2 being 0.51 and 0.55, respectively. R^2 values less than 0.65 during calibration and validation periods might be attributed to uncertainties related to the input data (e.g. rainfall, DEM etc.), model structure and parameterisations. For examples: IMD gridded ($0.25^\circ \times 0.25^\circ$) rainfall data used as input in the hydrological model was derived

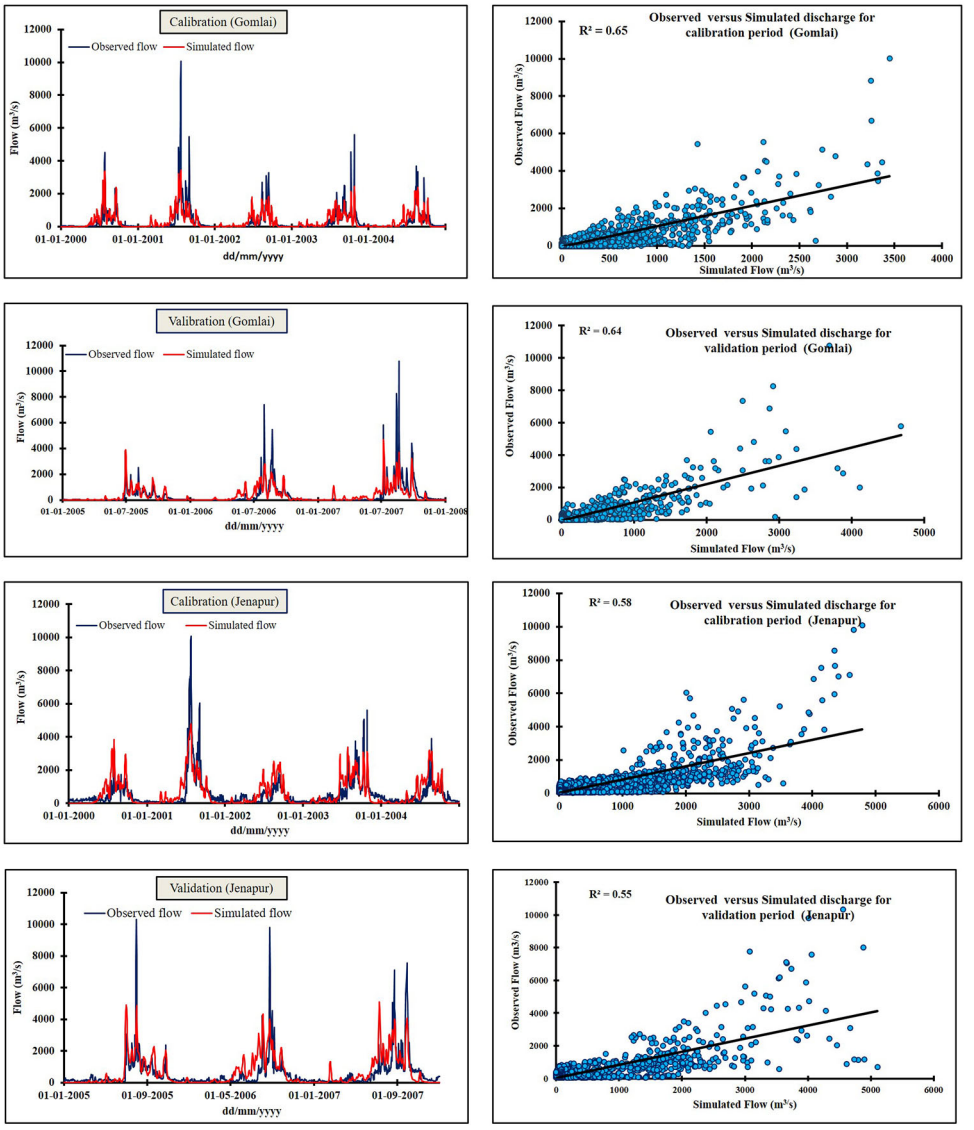

Figure 5. Comparison of observed and simulated discharge for calibration and validation period at Gomlai and Jenapur.

from interpolation of a gauge station data that was not recorded at the hydrological stations. Spatial interpolation of this rainfall data thus inherited uncertainty in its approximation. Further, the input DEM (a raster based grid data) is also an approximation of the true topographical characteristics of the basin. The accuracy of topographical and hydrological parameters derived from DEM is highly subjective to the size of its resolution. These uncertainties related to scale and approximations in system processes make HEC-HMS difficult to model exact hydrologic phenomena. Usually, a larger value of *NSE* than 0.4 and R^2 than 0.5 is considered satisfactory (Motovilov et al. 1999; Moriasi et al. 2007). After the calibration and validation, HEC-HMS model was used to simulate peak flows for floods with a 2-year, 10-year, 25-year, 50-year, and 100-year return period for LULC

changes scenarios of the year 1985 and 2018. These hydrographs were saved as time series data and used as an input into the HEC-RAS model for estimating flood inundation in the BRB.

4.3. Uncertainty estimation

Markov Chain Monte Carlo (MCMC) method that is based on Byes rule was used for estimating uncertainty associated with the HEC-HMS model (Schoups et al. 2010). It works by creating many alternative models of the watershed using an automated sampling procedure (https://www.hec.usace.army.mil/confluence/hmsdocs/hmsum/latest/assessing-model-uncertainty/uncertainty-analyses). Each sample is created by sampling the model parameters according to their individual probability distribution. Further, the sample is simulated to obtain a watershed response corresponding to the sampled parameter values. All responses from all the samples can be analysed statistically to evaluate the uncertainty in the simulated watershed response. The indices such as the percent of observations bracketed by the 90PPU (P-factor) and the relative width (R factor) are adopted for the uncertainty interval evaluation. The goodness of calibration and prediction uncertainties is judged on the basis of the closeness of the P-factor to 100% with the smallest possible R-factor. R-factor is estimate by following equation:

$$R-factor=\frac{\frac{1}{n}\sum_{t_i}^{n}\left(Q_{ti,95\%}^{M}-Q_{ti,5\%}^{M}\right)}{\sigma_{obs}} \tag{15}$$

where $Q_{ti,95\%}^{M}$ and $Q_{ti,5\%}^{M}$ is the upper and lower boundaries of predicted interval respectively, and σ_{obs} is the standard deviation of measured data. For this study, P- factor was 0.678 (67.8%) and R-factor was 0.91 that is in the acceptable range (Mousavi et al. 2012).

4.4. Hydraulic modelling using HEC-RAS model

HEC-RAS version 5.0.7 and HEC-GeoRAS version 10.2 (an ArcGIS extension) was used for hydraulic modelling and estimating inundated areas in the BRB. 1 D unsteady flow simulation was performed under the subcritical flow regime to derive water levels in the river networks. The equations (Horritt and Bates 2002) used in 1 D unsteady flow simulation are described as:

$$\frac{\partial A}{\partial t}+\frac{\partial \emptyset Q}{\partial x_c}+\frac{\partial (1-\emptyset)Q}{\partial x_f}=0 \tag{16}$$

$$\frac{\partial Q}{\partial t}+\frac{\partial}{\partial x_c}\left(\frac{\emptyset^2Q^2}{A_c}\right)+\frac{\partial}{\partial x_f}\left(\frac{(1-\emptyset)^2Q^2}{A_f}\right)+gA_c\left(\frac{\partial z}{\partial x_c}+S_c\right)+gA_f\left(\frac{\partial z}{\partial x_f}+S_f\right)=0 \tag{17}$$

$$\emptyset=\frac{K_c}{K_c+K_f} \tag{18}$$

where,

$$K=\frac{A^{5/3}}{nP^{2/3}},S_c=\frac{\emptyset^2Q^2n_c^2}{R_c^{4/3}A_c^2},S_f=\frac{(1-\emptyset^2)Q^2n_f^2}{R_f^{4/3}A_f^2} \tag{19}$$

where, Q is the total flow, A_c and A_f is the cross-sectional area for flow in channel and floodplain, respectively. x_c and x_f is distances along the channel and floodplain, P the

wetted perimeter, R the hydraulic radius (A/P), n the Manning's roughness value and S the friction slope. ϕ determines how flow is partitioned between the floodplain and channel, according to the conveyances Kc and K_f (Horritt and Bates 2002).

The different steps involved in the performance of the hydraulic analysis were grouped into three categories: pre-processing, processing, and post-processing. During the pre-processing stage, a TIN model of the BRB was generated from ASTER DEM data of the study area. Further, different geometric layers such as the stream centreline, flow path centrelines, bank lines, and cross-section cut lines were generated from the TIN using HEC-GeoRAS. All these geometric layers were created in the form of polylines. HEC-GeoRAS generates the cross-sectional cut lines automatically at a fixed, regular interval, which was further processed manually according to the need. These data were imported to HEC-RAS for processing. 1 D unsteady flow simulation was performed under the subcritical flow regime to derive water levels in the river networks. The simulation was carried out corresponding to the peak flows (hydrographs) of 2-year, 10-year, 25-year, 50-year and 100-year rerun periods. The peak flows, together with the boundary conditions, were put as inputs for the analysis of steady flow. Due to the subcritical flow regime, the boundary condition was determined at the downstream end of the river reach. The slope of the river bed was used as the boundary condition in normal depth. The simulation generated water surface elevations for the corresponding flood events of different return periods. The water level profiles of 2-year, 10-year, 25-year, 50-year and 100-year rerun periods and river centrelines were stored in Spatial Data Format (SDF) and exported to the ArcGIS for the post-processing. Inundation mapping was finally performed in two stages: generation of water surface and delineation of floodplain using raster. For the generation of water surface, TINs were created for floods with a 2-year, 10-year, 25-year, 50-year and 100-year return periods, using water surface elevation at each cross-section. The delineation of floodplain was performed using water surface TINs that generated in the previous step.

5. Results and discussion

5.1. Flood probability analysis

In this study, six commonly used probability distribution methods, e.g. Gumbel, Log-Pearson-III, Lognormal (3 P), Weibull, Normal and Exponential were tested to determine storm rainfall depths for various return periods. The return period or recurrence interval is a measure of how often extreme event of certain magnitude is likely to happen (Elsebaie 2012). However, based on the goodness of fit test analysis (Kolmogorov Smirnov, Chi-Squared and Anderson-Darling), Gumbel and Log-Pearson-III distributions were found to be best fitted among all of the above. Further owing to Gumbel's distribution suitability for modelling maxima (Haktanir 1992; Loaiciga and Leipnik 1999; Elsebaie 2012), it was finally selected to determine storm rainfall depths for various return periods within BRB.

The IMD daily rainfall data from 1981 to 2018 together with the Thiessen polygon method were used to determine the average rainfall over the basin. By using mean basin rainfall data of all the 38 years, 1-day annual maximum series was developed. From the developed 1-day annual maximum series, the extreme rainfall depths for 2-year, 10-year, 25-year, 50-year and 100-year return period were estimated using following equations (Gumbel 1941; Elsebaie 2012):

$$R_T = R_{Avg} + KS \tag{20}$$

where, K is Gumbel frequency factor defined as:

$$K = -\frac{\sqrt{6}}{\pi}\left[0.5772 + \ln\left(\ln\left(\frac{T}{T-1}\right)\right)\right] \tag{21}$$

where, R_T refers to rainfall (mm) for specific return period T (in year), R_{Avg} is the average of maximum rainfall corresponding to specific duration (for this study, 38 years) and S is the standard deviation. R_{Avg} is derived as per the equation given below:

$$R_{Avg} = \frac{1}{n}\sum_{i=n}^{n} R_i \tag{22}$$

where, R_i is individual maximum value of rainfall and n is the number event or year record. The standard deviation (S) is calculated by using the following equation.

$$S = \left[\frac{1}{n-1}\sum_{i=1}^{n}(R_i - R_{Avg})^{2.}\right]^{1/2} \tag{23}$$

The adequacy of the Gumbel's distribution was also evaluated through Anderson-Darling (A^2) goodness of fit test. The Cumulative Distribution Function (CDF) for the extreme rainfall events generated from the Gumbel distribution method was compared with the expected CDF. The equation used for estimating Anderson-Darling (A^2) goodness of fit test is given below:

$$A^2 = -n - \frac{1}{n}\sum_{i=1}^{n}(2i-1)*[lnF(X_i) + \ln(1 - F(X_{n-i+1}))] \tag{24}$$

where, $F(X_i)$ is CDF of ith sample (X_i) and n represents sample size. If the calculated value of A^2 given by the Gumbel probability distribution is less than the critical value at the given significance level, then distribution is considered to be suitable for analysis of 1-day annual maximum rainfall data (Kamal et al. 2017). The test statistic result was 0.63, which is less than critical value of 2.501 at 5% of signification level. This suggests that the Gumbel distribution method is suitable for frequency analysis of 1-day annual maximum rainfall data. Table 3 shows the estimated extreme rainfall depths for various return periods. It was 57.2, 80.6, 92.4, 101.2, and 109.8 mm for 2-year, 10-year, 25-year, 50-year and 100-year rerun periods, respectively. Flood hydrographs of 2-year, 10-year, 25-year, 50-year and 100-year rerun periods in the BRB were generated from these extreme rainfall values.

5.2. Classification of LULC and change detection

Maps of the LULC types of the BRB were prepared for the year 1985, 2005 and 2018 using multispectral optical satellite data from Landsat-4, Landsat-5 and Sentinel-2, respectively. The satellite images were acquired only between the pre-monsoon months of April and May to minimise the effects of the cloud covers. Maximum likelihood algorithm of supervised classification technique (Lillesand et al. 2015) was applied for defining LULC classes from the satellite data. The entire basin was grouped broadly into four LULC classes: forest cover, agriculture land, built-up land and water bodies. The areas covered by different LULC types are summarised in Table 4 for the years 1985, 2005 and 2018. Agriculture land (51.1% to 54.7%) and forest cover (39.7% to 45.4%) were found to be the most dominant LULC types in the BRB.

Table 3. Estimated rainfall and frequency factor for various return periods.

	Standard deviation (σ)	15.9 (mm)
	Average rainfall (R_{Avg})	59.8 (mm)
Return period (T) in years	Frequency Factor (K)	Rainfall (R_T) in mm
2	−0.2	57.2
10	1.3	80.6
25	2.0	92.4
50	2.6	101.2
100	3.1	109.8

Table 4. Percentage change in the LULC types over the BRB between 1985 and 2005, 2005 and 2018 and 1985 and 2018.

		Area in Km^2			AREA (%)			Change in LULC (%)		
S.No.	LULC class	1985	2005	2018	1985	2005	2018	1985–2005	2005–2018	1985–2018
1	Forest	17720.8	17004.1	15513.9	45.4	43.5	39.7	−4.0	−8.8	−12.5
2	Agricultural land	19965.9	20631.7	21370.5	51.1	52.9	54.7	3.3	3.6	7.0
3	Built-up land	230.7	286.9	1124.9	0.6	0.7	2.9	24.4	292.1	387.6
4	Water bodies	1127.6	1122.5	1035.9	2.9	2.9	2.7	−0.5	−7.7	−8.1
Total		39045.2	39045.2	39045.2	100	100	100			

The reliability of the classification results was checked through accuracy assessment. Error matrix (Stehman 1997) was applied for assessing accuracy of individual class as well as the overall classification. For 1985, 2005 and 2018 LULC maps, accuracy assessment results showed an overall accuracy of 78.7%, 83.6% and 86%, respectively and overall kappa statistic of the year 1985, 2005 and 2018 were 0.7, 0.8 and 0.8, respectively. The relatively lower overall accuracy and kappa accuracy in 1985 than 2005 and 2018 might be linked to the poor spatial resolution (56 m) of Landsat-4 data. However, among the individual classes, the highest (∼95%) and lowest producer accuracy was reported for the forest and built-up areas (∼65%) in 1985, respectively. With the improved spatial resolution (Sentinel-2A data), the producer accuracy for the built-up areas had increased to ∼87%.

The changes occurred in LULC patterns of the BRB from 1985 to 2005, 2005 to 2018, and 1985 to 2018 are shown in Table 4. The comparison of LULC maps of different years (1985 and 2018) revealed increase in the areas of the agricultural land and built-up land, and decline in the forest cover and the water bodies (Figure 6). During the 1985 and 2005 period, the area of built-up land and agricultural land increased by 24.3% and 3.3%, while a reduction of around 4% and 0.5% in forest and water bodies was observed. However, between 2005 and 2018, the increase in the built-upland and agricultural lands were 292.1% and 3.6%, respectively. The areas of forest cover and water bodies showed decrease of 8.8% and 7.7% for the same period. Thus, changes in the LULC patterns were relatively more rapid in nature from 2005 onwards. Overall, within last 33 years (1985–2018), there was an increment of 387.6% and 7.0% in built-up area and agriculture land, and 12.5% and 8.1% reduction in the forest and the waterbodies coverage, respectively. In 1985, total area under built-up land and agricultural land were 230.7 km^2 and 19965.9 km^2, which had expanded to 1124.9 km^2 and 21370.5 km^2 in 2018, respectively. Deforestation caused by the mining activities, and burning of the forest for agriculture in the eastern part of the upper catchment is the primary reasons for the reduction in forest cover (http://mowr.gov.in/sites/default/files/NWM_OR-FM-CC_2015_Vol-2_0.pdf). The region is bestowed mineral such as iron ore, copper, chromite, coal, manganese, limestone, dolomite, lead and bauxite etc., which has led to the set-up of several industries in the basin. The first steel plant, Rourkela Steel Plant, was established in 1955 with the collaboration from Germany. At present, there are

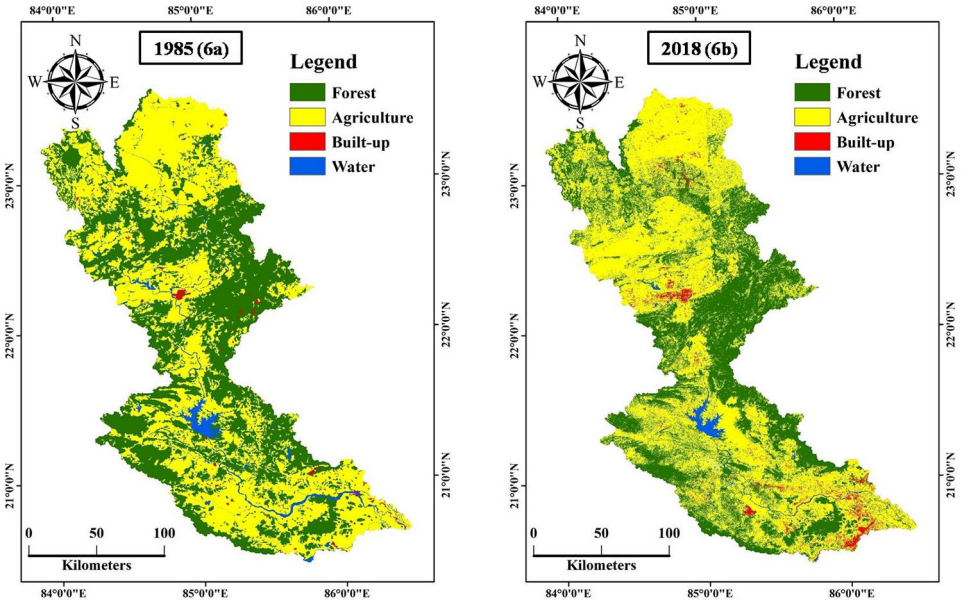

Figure 6. Maps showing areas covered by different LULC types in the BRB for 1985 (6a) and 2018 (6 b).

three major industrial belts: Raigarh industrial belt, Rourkela industrial belt and Angul-Talcher industrial belt. The world's second largest sponge iron plant (Jindal Steel and Power Ltd.) is located in the Raigarh district of Chattisgarah. The development in industries has also increased infrastructures such as roads, railway lines, housing societies, hospital and schools, leading to the expansion of built-up areas in the catchment. Further, the construction of Rengali dam in 1985, and other minor irrigation projects afterwards have greatly improved irrigation facilities downstream. This has resulted into the expansion of agricultural lands in the BRB. Manning's n-values were also derived from the LULC maps. The noted values were: 0.10 for the forest cover, 0.05 for the agricultural land, 0.12 for the built-up land and 0.03 for the water bodies.

5.3. Influence of changes in LULC types on the flood hydrograph

The impacts of changes in LULC between 1985 and 2018 on the flood peak discharge were analysed in the BRB for the floods of various return periods. The developed HEC-HMS model used SCS-CN loss method for simulating runoff from the floods of 2-year, 10-year, 25-year, 50-year and 100-year rerun periods. SCS-CN map for the BRB was prepared for the year 1985 and 2018 from the digitally classified satellite image (LULC maps), DEM and HSGs maps (Figure 7). It was used to estimate infiltration losses in the BRB. The CN values assigned to individual LULC class and soil group is shown in Figure 7. CN values ranged from 70 to 77 in forest cover, 82 to 85 in the agricultural lands, 90 to 92 in the built-up lands and 100 in the water bodies. Among the classes, the forest cover was marked with the lowest CN values (70 to 77), indicating the highest infiltration rate and lowest surface runoff. Arsyad (2019) and Marie Mireille et al. (2019) also reached on similar conclusions through their studies conducted in the teaching forest of Hasanuddin University (Maros Regency) and Narok County (Kenya), respectively. The infiltration rate for a LULC class is determined by the slope, intensity of rainfall and

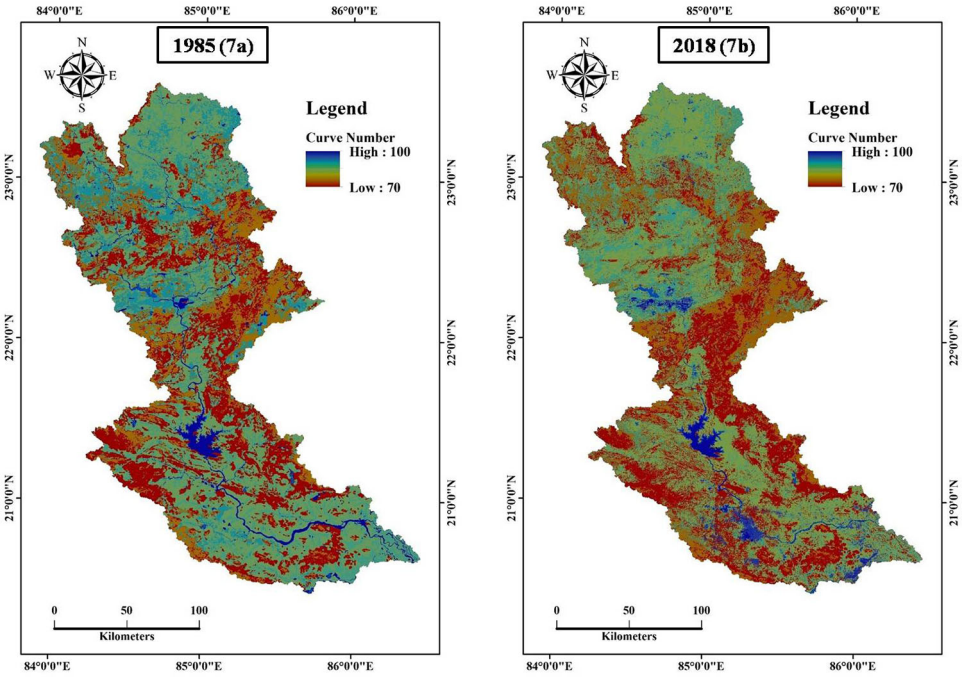

Figure 7. Spatial pattern of variations in SCS-CN values in the BRB is shown for 1985 (7a) and 2018 (7 b).

physical characteristics of the underlying soil groups (Halwatura and Najim 2013). The slope in the BRB varies from ∼0° to 70° within forest cover, from ∼0° to 55° within agricultural land and from ∼0° to 50° within built-up lands. The major soils in the BRB are from C and D groups of HSGs. The water retention capacity in such soils are very high due to their poor hydraulic conductivity (≤10.µm/s to >1.0 µm/s for C group and ≤1.0 µm/s for D group). Therefore, BRB as a large was marked with the high surface runoff potential. A composite CN was also derived for each sub-basin using weighed average method (Feldman 2000; Satheesh Kumar et al. 2017).

Figure 8 illustrates the flood hydrographs generated at the outlet point of the basin (Jenapur) for the floods of 2-year, 10-year, 25-year, 50-year and 100-year rerun periods under LULC change scenarios of the year 1985 and 2018. The change in peak flows of the floods with 2-year, 10-year, 25-year, 50-year and 100-year rerun periods for the LULC change scenarios of the year 1985 and 2018 is presented in Table 5. The comparison of peak flows revealed that the volume of peak discharge had increased by 10%, 7.2%, 6.4%, 5.9% and 5.4% for the flood events of 2-year, 10-year, 25-year, 50-year and 100-year rerun periods in 2018. The increase was relatively greater for the lower return period of 2-years than the higher return period of 100-years. Over the past 33 years, the increase in peak runoff for the 100-year return period varied around 5.4% compared to 10.0% for 2-year return. The rise in the peak flow related with the flood events in 2018 are related with decline in forest cover area of the BRB. The forest cover declined from 17720.8 km^2 in 1985 to 15513.9 km^2 in 2018; resulting a total loss of 2206.9 km^2 in its area. The decrease in forest cover generally causes increase in surface runoff as well as rise in the peak flow of the river (Hassaballah et al. 2017). Guzha et al. (2018) reviewed 37 catchments in East Africa to investigate effects of LULC changes on surface runoff and concluded that surface runoff had increased by 45 ± 14% because of the deforestation in the catchments. In another study by Berihun et al. (2019), it was observed that changes in LULC had intensified hydrological responses of the

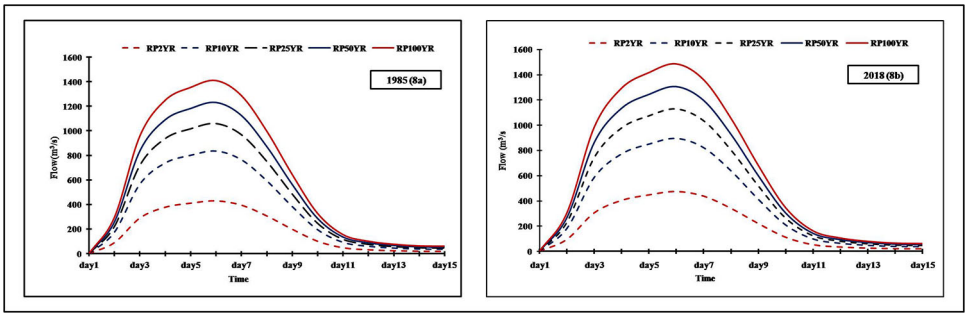

Figure 8. Flood hydrographs generated at the outlet point of the basin (Jenapur) using HEC-HMS for the floods of various return periods under LULC change scenarios of the year 1985 (8a) and 2018 (8 b).

Table 5. HEC-HMS simulated peak discharge and inundated areas in BRB at Jenapur for floods of different return periods ubased on the LULC types of 1985 and 2018.

Return period (Year)	Peak discharge (m^3/s)		Percentage (%) change in peak discharge *w.r.t.* 1985	Inundated area (km^2)		Percentage (%) change in inundated areas *w.r.t.* 1985
	LULC 1985	LULC 2018		LULC 1985	LULC 2018	
2	431.6	474.9	10.0	475.5	614.1	29.1
10	835.9	896.2	7.2	612.2	778.7	27.2
25	1060.1	1127.6	6.4	680.7	820.2	17
50	1233	1305.2	5.9	729.6	868.2	19
100	1409	1485.5	5.4	758.3	885.6	16.8

watersheds resulting increase in surface runoff ranging from 4% to 28.7%. Additionally, this decrease in the forest cover area was compensated with the increased proportion of agricultural and built-up lands. From 1985 to 2018, the agricultural and built-up area increased by 1404.6 km^2 and 894.2 km^2, respectively. The expansion in built-up land has increased impermeable surfaces in the basin, leading to the low infiltration rate and high overflow. The outcomes of this study agree with the findings of the earlier studies conducted in other basins (Wan and Yang 2007; Zope et al. 2016; Hu and Shrestha 2020).

5.4. The extent of floods according to the LULC types of 1985 and 2018

The flood inundation maps of 1985 and 2018 in the study area under changing LULC scenarios (1985 and 2018) were prepared using HEC-RAS model from the simulated flood hydrograph of 2-year, 10-year, 25-year, 50-year and 100-year rerun periods. Figures 9 and 10 shows modelled flooded areas in 1985 and 2018, respectively. The modelled inundated areas under LULC conditions of 1985 for the floods of 2-year, 10-year, 25-year, 50-year and 100-year rerun periods were 475.5 km^2, 612.2 km^2, 680.7 km^2, 729.6 km^2 and 758.3 km^2, respectively. However, it was 614.1 km^2, 778.7 km^2, 820.2 km^2, 868.2 km^2 and 885.6 km^2 under the LULC conditions of 2018. Thus, flood inundated areas recorded increase under LULC conditions of 2018 as compared of 1985. The increase was 22.6% for the floods of 2-year return period and 14.4% for 100 year return period. The lower catchment which has been characterised with intensive agriculture and high population density is highly susceptible to flooding than upstream due to the low elevation (7–100 m) and slope.

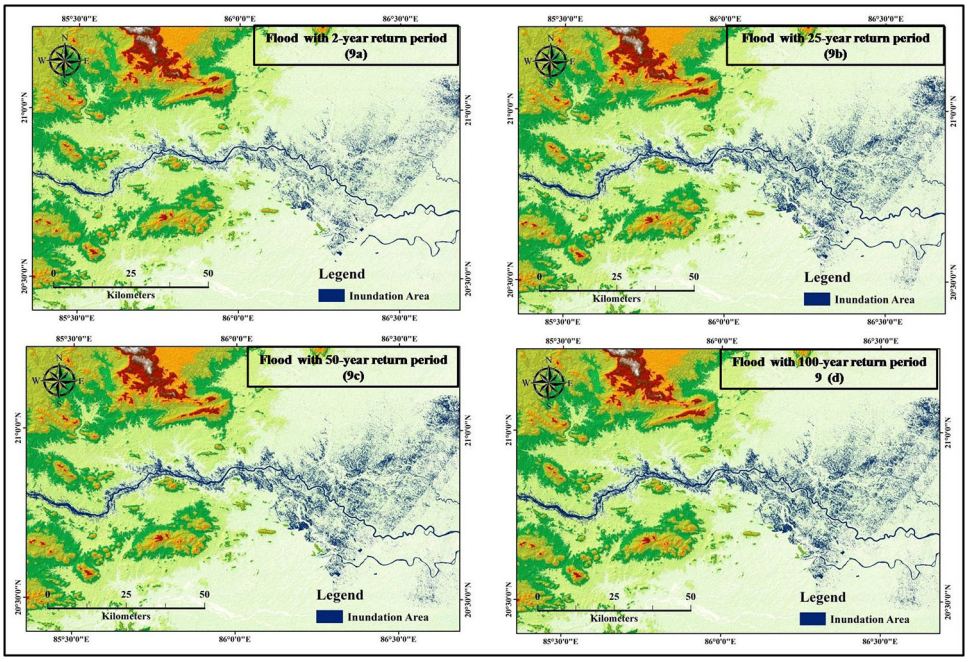

Figure 9. HEC-RAS simulated flood inundated areas under LULC conditions of 1985 for the floods with 2-year (9a), 25-year (9 b), 50-year (9c) and 100-year (9d) rerun periods.

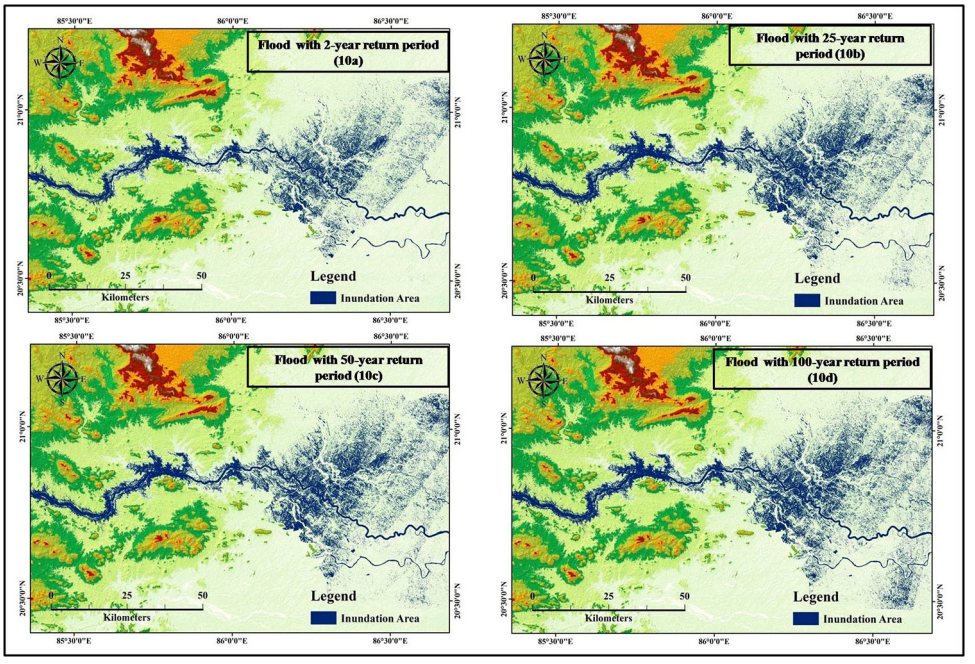

Figure 10. HEC-RAS simulated flood inundated areas under LULC conditions of 2018 for the floods with 2-year (10a), 25-year (10 b), 50-year (10c) and 100-year (10d) rerun periods.

Table 6. HEC-HMS simulated peak discharge in BRB at Jenapur for floods of different return periods in 2080s (2071–2100) under climate change scenarios SSP245 and SSP585.

	Peak discharge (m^3/s)				
		SSP245 (2080s)		SSP585 (2080s)	
Return period (Year)	2018	EC-Earth3	MRI-ESM2	EC-Earth3	MRI-ESM2
2	474.9	1165.2	886.6	1936.1	1137
10	896.2	2129.7	2140.9	3699.9	2446.7
25	1127.6	2594.8	3143.8	4617.6	2818.2
50	1305.2	3024.9	3331.3	5305.7	3669.7
100	1485.5	3411.5	3846.9	5992.9	4197.6

5.5. Impacts of climate change on flooding

To understand the impacts of climate change on fluvial flooding, the peak flows generated based on the outputs of the two CMIP6 GCMs, i.e. EC-Earth3 and MRI-ESM2, forced using the SSP245 and SSP585 GHG emission scenarios, were used for the future floods of various return periods. The outputs from the CMIP6 models are likely to be more realistic than those from previous generations of the IPCC models, i.e. CMIP3 and CMIP5, given their significant improvement in simulating extreme precipitation events in historical records, which are key to the occurrence of flooding (Kim et al. 2020). Table 6 illustrates the peak flows for floods with a 2-year, 10-year, 25-year, 50-year and a 100-year return period for the 2080s (2071–2100) under SSP245 and SSP585. The comparison (with respect to 2018) of peak flow revealed that the volume of peak discharge would increase in future for all return periods under both the scenarios. The increase would be much greater under SSP585 (∼139% to 312%) for all return periods than SSP245 (∼86% to 155%) in both the models. Between the models, the highest increase in peak flow of floods for all return periods was projected under EC-Earth3 than MRI-ESM2 for SSP585. Moreover, the increase was higher for the lower return period of 2-years than the higher return period of 100-years under EC-Earth3 model. Opposite to this, MRI-ESM2 predicted relatively greater increase for the higher return period of 100-years than the lower return period of 2-years. The increase in peak flows for the 100-year return period varied around 129% to 303% compared to 86% to 307% for 2-year return. Such increase in peak flows of the floods for different return periods might be attributed to the increased intensity and amount of future rainfall events (Krishnan et al. 2020; Sanjay et al. 2020a).

Figures 11 and 12 show the modelled flooded areas with floods of various return periods in 2080s under SSP245 and SSP585, respectively. The inundated areas under SSP245 scenario of MRI-ESM2 model for the floods of 2-year, 10-year, 25-year, 50-year and 100-year rerun periods were projected to be 1068.7 km^2, 1476.2 km^2, 1880.6 km^2, 1946.9 km^2 and 2206.4 km^2, respectively. However, it would be 1118.3 km^2, 1649.9 km^2, 1775.9 km^2, 2132.1 km^2 and 2264.6 km^2 under the scenario of SSP585. Similarly, the modelled inundated areas under SSP245 scenario of EC-Earth3 model were projected to be 1124.3 km^2, 1471.4 km^2, 1725.4 km^2, 1820.3 km^2 and 1984.8 km^2 with the floods of 2-year, 10-year, 25-year, 50-year and 100-year rerun periods, respectively. The modelled areas inundated under scenario of SSP585 for the floods of 2-year, 10-year, 25-year, 50-year and 100-year rerun periods were 1389.1 km^2, 2156.6 km^2, 2321.4 km^2, 2472.9 km^2 and 2698.6 km^2, respectively. Thus, flood inundated areas recorded increase under climate change scenarios for both the models in 2080s as compared of 2018. The increase was in range of ∼9% to 41%to for the floods of 2-year return period and ∼82% to 148% for a100-year return period.

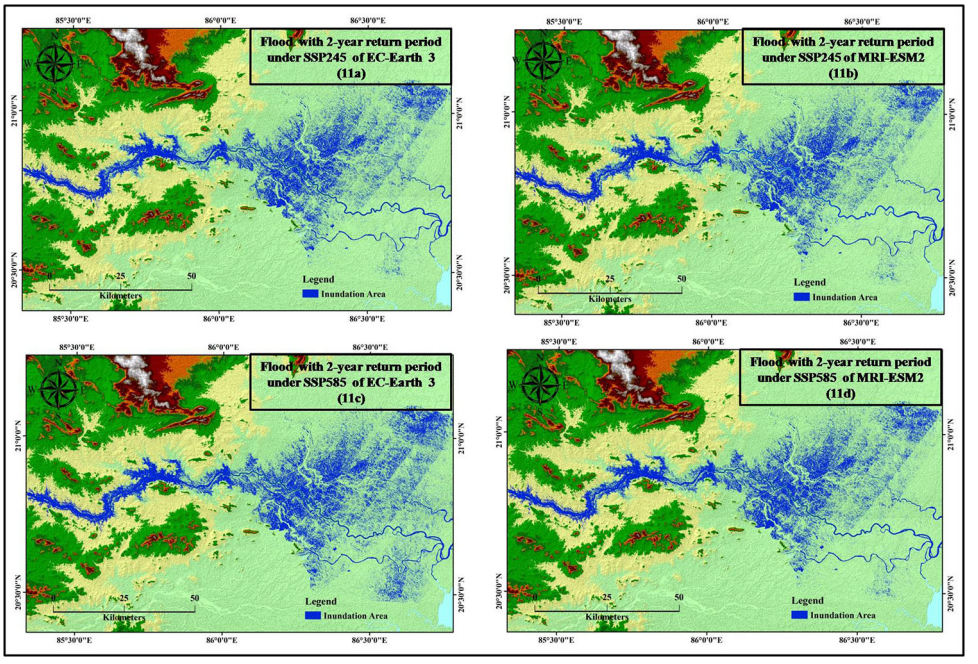

Figure 11. HEC-RAS simulated flood inundated areas with floods of 2-year return period for EC-Earth3 and MRI-ESM2 models in 2080s under SSP245 (11a and 11 b) and SSP 585 (11c and 11 d) scenarios.

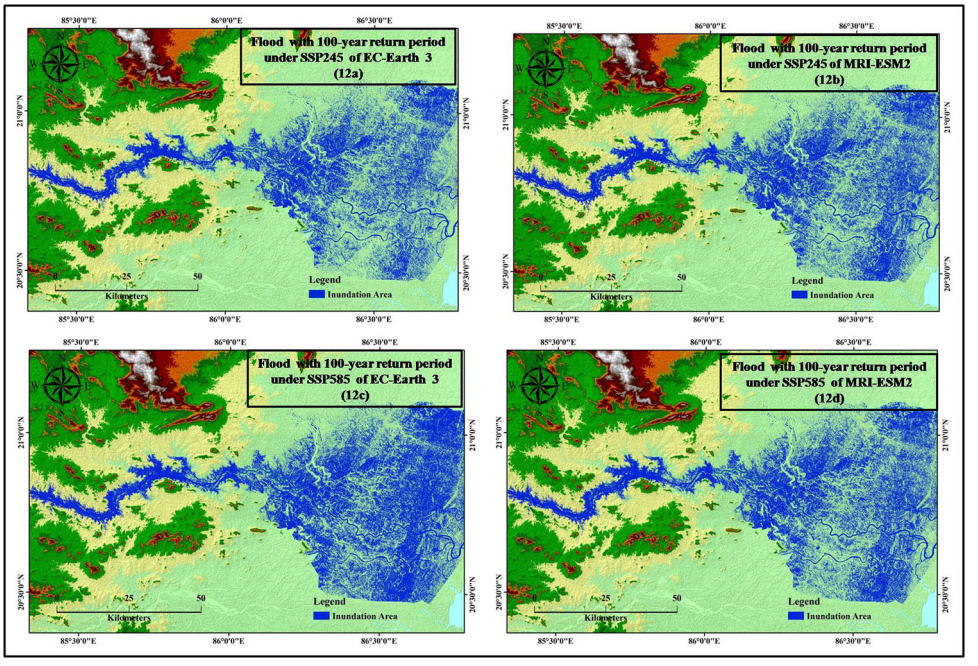

Figure 12. HEC-RAS simulated flood inundated areas with floods of 100-year return period for EC-Earth3 and MRI-ESM2 models in 2080s under SSP245 (12a and 12 b) and SSP 585 (12c and 12 d) scenarios.

6. Conclusions

This study examined the impacts of changes in LULC, as observed between 1985 and 2018, and future climate change for the 2080s (2071–2100) on peak discharge over the BRB in eastern India and subsequently fluvial flooding for floods of a 2-year, 10-year, 25-year, 50-year and 100-year return period. Between 1985 and 2018, the BRB experienced deforestation as a result of an intensification of agriculture, population growth and urbanisation. Accordingly, during that period, the surface area covered by agricultural land and built-up areas increased from approximately 19,965 km^2 to 21,370 km^2 (seven percent) and from about 231 km^2 to 1125 km^2 (387%), respectively, on the one hand, while on the other hand, the area covered by forests decreased from approximately 17721 km^2 to 15514 km^2, a loss of almost 220 km^2 (12.5%). Mining and the burning of the forests for agriculture in the eastern part of the upper catchment are the main reasons for deforestation.

The conversion of forested land to agriculture has led to significant increases in both peak discharge and the areas prone to inundation. The comparison of peak flows revealed that the volume of peak discharge increased by 10%, 7.2%, 6.4%, 5.9% and 5.4% for floods with a return period of 2-year, 10-year, 25-year, 50-year and 100-year in 2018 than 1985. The increase was relatively higher for the lower return period of 2-years than the high return period of 100-years. Over the past 33 years, the increase in peak runoff for the 100-year return period varied around 5.4% compared to 10.0% for 2-year return. Moreover, the inundated areas modelled under LULC conditions of 2018 were relatively extensive than the LUCL conditions of 1985. It was also established that the percentage change in the flood extent area during the three decades (1985–2018), is marginally more for the lower return periods as compared to that of the higher return periods. An increase in floods with a 2-year, 10-year, 25-year, 50-year and 100-year return period is also projected for the 2080s under both SSP245 and SSP585. The increase would be much greater under SSP585 for all return periods than SSP245 (4.5 W/m^2) owing to the higher radiating forcing under scenario of SSP585 (8.5 W/m^2). The likelihood that such flooding will further increase according to climate change scenarios, mitigative measures will be required and that such measures should integrate both structural and non-structural approaches. This is because the former significantly alter the natural environment of the river, resulting in the loss of habitat etc. This knowledge will help to plan future development and mitigate the risk of flooding in the BRB.

Notes

1. http://gdem.ersdac.jspacesystems.or.jp/.
2. http://mowr.gov.in/sites/default/files/NWM_OR-FM-CC_2015_Vol-2_0.pdf
3. https://indiawris.gov.in/wris
4. http://gdem.ersdac.jspacesystems.or.jp/
5. https://earthexplorer.usgs.gov/.
6. https://daac.ornl.gov/get_data/.
7. https://zenodo.org/record/3874046#.YBei_XPivIW

Acknowledgments

The authors acknowledge both the India Water Resources Information System (WRIS) (https://indiawris.gov.in/wris) and India Meteorological Department (IMD) for providing, at no cost, the hydrological and climatological data used in this study. We also thank the Indian Institute of Technology (IIT) - Gandhinagar for the downscaled and bias corrected CMIP6 projections, available at https://zenodo.org/

record/3874046#.YBei_XPivIW, over the study river basin, as well as the United States Geological Survey (USGS) Earth Explorer (https://earthexplorer.usgs.gov/) for the Landsat data and the Oak Ridge National Laboratory Distributed Active Archive Centre (DAAC) (https://daac.ornl.gov/get_data/) for the digital soil map used in this paper. In addition, we extend our gratitude to the Regional Editor and the two anonymous reviewers for their constructive comments, which helped improved the quality of the manuscript.

Disclosure statement

No potential conflict of interest was reported by the authors.

Funding

This research did not receive any specific grant from funding agencies in the public, commercial, or not-for-profit sectors.

References

Abdessamed D, Abderrazak B. 2019. Coupling HEC-RAS and HEC-HMS in rainfall–runoff modeling and evaluating floodplain inundation maps in arid environments: case study of Ain Sefra city, Ksour Mountain. SW of Algeria. Environ Earth Sci. 78(19):586.

Alfieri L, Burek P, Feyen L, Forzieri G. 2015. Global warming increases the frequency of river floods in Europe. Hydrol Earth Syst Sci. 19(5):2247–2260.

Andréassian V. 2004. Waters and forests: from historical controversy to scientific debate. J Hydrol. 291(1-2):1–27.

Arsyad U. 2019. The characteristics of infiltration in natural forest in teaching forest of Hasanuddin University University at Maros Regency In: IOP Conference Series: Earth and Environmental Science, Vol. 270, No. 1, p. 012004. IOP Publishing.

Berihun ML, Tsunekawa A, Haregeweyn N, Meshesha DT, Adgo E, Tsubo M, Masunaga T, Fenta AA, Sultan D, Yibeltal M, et al. 2019. Hydrological responses to land use/land cover change and climate variability in contrasting agro-ecological environments of the Upper Blue Nile basin, Ethiopia. Sci Total Environ. 689:347–365.

Beschta RL, Pyles MR, Skaugset AE, Surfleet CG. 2000. Peakflow responses to forest practices in the western cascades of Oregon, USA. J Hydrol. 233(1–4):102–120.

Bharat S, Mishra V. 2021. Runoff sensitivity of Indian sub-continental river basins. Sci Total Environ. 766:142642.

Bosch JM, Hewlett JD. 1982. A review of catchment experiments to determine the effect of vegetation changes on water yield and evapotranspiration. J Hydrol. 55(1–4):3–23.

Brivio PA, Colombo R, Maggi M, Tomasoni R. 2002. Integration of remote sensing data and GIS for accurate mapping of flooded areas. Int J Remote Sens. 23(3):429–441.

Chow VT, Maidment DR, Mays LW. 1988. Applied hydrology. New York (NY): McGraw-Hill.

CPSP Report. 2015. Water resources assessment of Brahmani River Basin, India. Country Policy Support Programme funded by Sustainable Economic Development Department National Policy Environment Division The Govt. of The Netherlands (Activity No. WW138714/DDE0014311).

Dahm RJ, Sperna Weiland FC, Singh UK, Lal M, Marchand M, Singh SK, Singh MP. 2019. Assessment of future rainfall for the Brahmani-Baitarani river basin–practical implications of limited data availability. J Water Clim Change. 10(4):782–798.

Dang ATN, Kumar L. 2017. Application of remote sensing and GIS-based hydrological modelling for flood risk analysis: a case study of District 8, Ho Chi Minh city, Vietnam. Geomatics Nat Hazards Risk. 8(2):1792–1811.

Déry SJ, Hernández Henríquez MA, Burford JE, Wood EF. 2009. Observational evidence of an intensifying hydrological cycle in northern Canada. Geophys Res Lett. 36(13):L13402.

Dhar ON, Nandargi S. 2003. Hydrometeorological aspects of floods in India. Nat Hazard 28(1):1–33.

Elsebaie IH. 2012. Developing rainfall intensity–duration–frequency relationship for two regions in Saudi Arabia. J King Saud Univ Eng Sci. 24(2):131–140.

EM-DAT. 2020. The OFDA/CRED international disaster database. [accessed 2020 July 20]. www.em-dat.ne.

Feldman AD. 2000. Hydrologic modeling system HEC-HMS: technical reference manual US Army Corps of Engineers, Hydrologic Engineering Center. [accessed 2020 July 20]. https://www.hec.usace.army.mil/software/hec-hms/documentation/HEC-HMS_Technical.ReferenceManual_(CPD-74B).pdf.

Forte F, Strobl RO, Pennetta L. 2006. A methodology using GIS aerial photos and remote sensing for loss estimation and flood vulnerability analysis in the Supersano-Ruffano-Nociglia Graben, Southern Italy. Environ Geol. 50(4):581–594.

Frey H, Haeberli W, Linsbauer A, Huggel C, Paul F. 2010. A multi-level strategy for anticipating future glacier lake formation and associated hazard potentials. Nat Hazards Earth Syst Sci. 10(2):339–352.

Gómez-Palacios D, Torres MA, Reinoso E. 2017. Flood mapping through principal component analysis of multitemporal satellite imagery considering the alteration of water spectral properties due to turbidity conditions. Geomatics Nat Hazards Risk. 8(2):607–623.

Gumbel EJ. 1941. The return period of flood flows. Ann Math Statist. 12(2):163–190.

Guzha AC, Rufino MC, Okoth S, Jacobs S, Nóbrega RLB. 2018. Impacts of land use and land cover change on surface runoff, discharge and low flows: evidence from East Africa. J Hydrol Reg Stud. 15: 49–67.

Haktanir T. 1992. Comparison of various flood frequency distributions using annual flood peaks data of rivers in Anatolia. J Hydrol. 136(1–4):1–31. (92)90002-D.

Halwatura D, Najim MMM. 2013. Application of the HEC-HMS model for runoff simulation in a tropical catchment. Environ Modell Softw. 46:155–162.

Hassaballah K, Mohamed Y, Uhlenbrook S, Biro K. 2017. Analysis of streamflow response to land use and land cover changes using satellite data and hydrological modelling: case study of Dinder and Rahad tributaries of the Blue Nile (Ethiopia–Sudan). Hydrol Earth Syst Sci. 21(10):5217–5242.

Hawker L, Bates P, Neal J, Rougier J. 2018. Perspectives on digital elevation model (DEM) simulation for flood modeling in the absence of a high-accuracy open access global DEM. Front Earth Sci. 6:233.

Horritt MS, Bates PD. 2002. Evaluation of 1D and 2D numerical models for predicting river flood inundation. J Hydrol. 268(1-4):87–99.

Hu P, Zhang Q, Shi P, Chen B, Fang J. 2018. Flood-induced mortality across the globe: Spatiotemporal pattern and influencing factors. Sci Total Environ. 643:171–182.

Hu S, Shrestha P. 2020. Examine the impact of land use and land cover changes on peak discharges of a watershed in the midwestern United States using the HEC-HMS model. Appl Geogr. 6(2):101–118.

Islam A, Sikka AK, Saha B, Singh A. 2012. Streamflow response to climate change in the Brahmani River Basin, India. Water Resour Manage. 26(6):1409–1424.

Jain V, Beyene M, Varay LS, Wasson RJ, Jain S. 2019. Riverine flood hazard: Part A types, processes and causative factors. Proc Indian Natl Sci Acad. 85(1):43–64.

Kamal V, Mukherjee S, Singh P, Sen R, Vishwakarma CA, Sajadi P, Asthana H, Rena V. 2017. Flood frequency analysis of Ganga River at Haridwar and Garhmukteshwar. Appl Water Sci. 7(4):1979–1986.

Kim YH, Min SK, Zhang X, Sillmann J, Sandstad M. 2020. Evaluation of the CMIP6 multi-model ensemble for climate extreme indices. Weather Clim Extreme. 29:100269.

Kjeldsen TR. 2010. Modelling the impact of urbanization on flood frequency relationships in the UK. Hydrol Res. 41(5):391–405.

Knebl MR, Yang ZL, Hutchison K, Maidment DR. 2005. Regional scale flood modeling using NEXRAD rainfall, GIS, and HEC-HMS/RAS: a case study for the San Antonio River Basin Summer 2002 storm event. J Environ Manage. 75(4):325–336.

Krishnan R, Sanjay J, Gnanaseelan C, Mujumdar M, Kulkarni A, Chakraborty S. 2020. Assessment of climate change over the Indian region: A report of the Ministry of Earth Sciences (MoES), Government of India. Springer Nature.

Lillesand T, Kiefer RW, Chipman J. 2015. Remote sensing and image interpretation. Danvers (USA): John Wiley & Sons.

Loaiciga HA, Leipnik RB. 1999. Analysis of extreme hydrologic events with Gumbel distributions: marginal and additive cases. Stochastic Environ Res Risk Assess. 13(4):251–259.

Marie Mireille N, M Mwangi H, K Mwangi J, Mwangi Gathenya J. 2019. Analysis of land use change and its impact on the hydrology of kakia and esamburmbur sub-watersheds of Narok County, Kenya. Hydrology. 6(4):86.

Maske SJ, Day JS. 1975. Unprecedented floods of August 1975 in Orissa. Indian J Meteorol Hydrol Geophys. 28(3):328–334.

Merwade V, Olivera F, Arabi M, Edleman S. 2008. Uncertainty in flood inundation mapping: current issues and future directions. J Hydrol Eng. 13(7):608–620.

Merz B, Thieken AH, Gocht M. 2007. Flood risk mapping at the local scale: concepts and challenges. In Flood risk management in Europe. Dordrecht: Springer. p. 231–251.

Miller JD, Hutchins M. 2017. The impacts of urbanisation and climate change on urban flooding and urban water quality: A review of the evidence concerning the United Kingdom. J Hydrol Reg Stud. 12: 345–362.
Mishra V, Bhatia U, Tiwari AD. 2020. Bias-corrected climate projections for South Asia from coupled model intercomparison project-6. Sci Data. 7(1):338.
Mokhtar ES, Pradhan B, Shafri HZM. 2018. Assessing flood inundation mapping through estimated discharge using GIS and HEC-RAS model. Arab J Geosci. 11(21):682.
Moriasi DN, Arnold JG, Van Liew MW, Bingner RL, Harmel RD, Veith TL. 2007. Model evaluation guidelines for systematic quantification of accuracy in watershed simulations. Trans ASABE. 50(3): 885–900.
Motovilov YG, Gottschalk L, Engeland K, Rodhe A. 1999. Validation of a distributed hydrological model against spatial observations. Agric Meteorol. 98–99:257–277.
Mousavi SJ, Abbaspour KC, Kamali B, Amini M, Yang H. 2012. Uncertainty-based automatic calibration of HEC-HMS model using sequential uncertainty fitting approach. J Hydroinformatics. 14(2):286–309.
Nash JE, Sutcliffe JV. 1970. River flow forecasting through conceptual models part I—A discussion of principles. J Hydrol. 10(3):282–290.
Patro S, Chatterjee C, Mohanty S, Singh R, Raghuwanshi NS. 2009. Flood inundation modeling using MIKE FLOOD and remote sensing data. J Indian Soc Remote Sens. 37(1):107–118.
Pradhan B. 2010. Flood susceptible mapping and risk area delineation using logistic regression, GIS and remote sensing. J Spatial Hydrol. 9(2):1–18.
Pramanik N, Panda RK, Sen D. 2010. One dimensional hydrodynamic modeling of river flow using DEM extracted river cross-sections. Water Resour Manage. 24(5):835–852.
Quirós E, Gagnon AS. 2020. Validation of flood risk maps using open source optical and radar satellite imagery. Trans GIS. 24(5):1208–1226.
Rai PK, Dhanya CT, Chahar BR. 2018. Coupling of 1D models (SWAT and SWMM) with 2D model (iRIC) for mapping inundation in Brahmani and Baitarani river delta. Nat Hazards. 92(3):1821–1840.
Ramankutty N, Foley JA. 1999. Estimating historical changes in global land cover: Croplands from 1700 to 1992. Global Biogeochem Cycles. 13(4):997–1027.
Ross CW, Prihodko L, Anchang J, Kumar S, Ji W, Hanan NP. 2018. HYSOGs250m, global gridded hydrologic soil groups for curve-number-based runoff modeling. Sci Data. 5:180091.
Saghafian B, Farazjoo H, Bozorgy B, Yazdandoost F. 2008. Flood intensification due to changes in land use. Water Resour Manage. 22(8):1051–1067.
Sanjay J, Krishnan R, Ramarao MVS, M, Singh BB, Patel J, Ingle S, Bhaskar P, Revadekar JV, Sabin TP, Mujumdar M. 2020a. Future climate change projections over the Indian region. *arXiv preprint arXiv: 2012.10386*.
Sanjay J, Ramarao MVS, Mahesh R, Ingle S, Singh BB, Krishnan R. 2020b. Regional climate change datasets for South Asia. *arXiv preprint arXiv:2012.10387*.
Sanyal J, Densmore AL, Carbonneau P. 2014. Analysing the effect of land-use/cover changes at sub-catchment levels on downstream flood peaks: A semi-distributed modelling approach with sparse data. Catena. 118:28–40.
Sanyal J, Lu XX. 2004. Application of remote sensing in flood management with special reference to monsoon Asia: a review. Nat Hazard. 33(2):283–301.
Satheesh Kumar S, Venkateswaran S, Kannan R. 2017. Rainfall–runoff estimation using SCS–CN and GIS approach in the Pappiredipatti watershed of the Vaniyar sub basin, South India. Model Earth Syst Environ. 3(1):24.
Schiermeier Q. 2011. Increased flood risk linked to global warming: likelihood of extreme rainfall may have been doubled by rising greenhouse-gas levels. Nature. 470(7334):316–317.
Schoups G, Vrugt JA, Fenicia F, Van De Giesen NC. 2010. Corruption of accuracy and efficiency of Markov chain Monte Carlo simulation by inaccurate numerical implementation of conceptual hydrologic models. Water Resour Res. 46(10):W10530.
Shafapour Tehrany M, Kumar L, Neamah Jebur M, Shabani F. 2019. Evaluating the application of the statistical index method in flood susceptibility mapping and its comparison with frequency ratio and logistic regression methods. Geomatics Nat Hazards Risk. 10(1):79–101.
Shi PJ, Yuan Y, Zheng J, Wang JA, Ge Y, Qiu GY. 2007. The effect of land use/cover change on surface runoff in Shenzhen region, China. Catena. 69(1):31–35.
Sindhu K, Durga Rao KHV. 2017. Hydrological and hydrodynamic modeling for flood damage mitigation in Brahmani–Baitarani River Basin, India. Geocarto Int. 32(9):1004–1016.

Singh BB, Singh M, Singh D. 2021. An overview of climate change over South Asia: observations, projections, and recent advances. In Singh RB, Chatterjee S, Mishra M, de Lucena AJ, editors. Practices in regional science and sustainable regional development. Singapore: Springer.
Singh D, Glupta RD, Jain S. 2015a. Statistical analysis of long term spatial and temporal trends of temperature parameters over Sutlej river basin, India. J Earth Syst Sci. 124(1):17–35.
Singh D, Jain SK, Gupta RD. 2015b. Statistical downscaling and projection of future temperature and precipitation change in middle catchment of Sutlej River Basin, India. J Earth Syst Sci. 124(4):843–860.
Singh DS, Awasthi A. 2011. Natural hazards in the Ghaghara River area Ganga Plain India. Nat Hazards. 57(2):213–225.
Smith MJ, Clark CD. 2005. Methods for the visualization of digital elevation models for landform mapping. Earth Surf Process Landforms. 30(7):885–900.
Stehman SV. 1997. Selecting and interpreting measures of thematic classification accuracy. Remote Sens Environ. 62(1):77–89. (97)00083-7.
Subramanya K. 2008. Engineering hydrology, New Delhi.
Vandana K, Islam A, Sarthi PP, Sikka AK, Kapil H. 2019. Assessment of potential impact of climate change on streamflow: a case study of the Brahmani River basin, India. J Water Clim Change. 10(3): 624–641.
Veach V, Moilanen A, Di Minin E. 2017. Threats from urban expansion, agricultural transformation and forest loss on global conservation priority areas. PLoS One. 12(11):e0188397.
Wallemacq P, Below R, McLean D. 2018. UNISDR and CRED report: Economic losses poverty & disasters (1998–2017). CRED, Brussels. CRED_Economic_Losses_10oct.pdf.
Wallemacq P, Guha-Sapir D, McClean D, CRED U. 1995. The human cost of weather related disasters. [assessed 2020 August 16].
Wan R, Yang G. 2007. Influence of land use/cover change on storm runoff—A case study of Xitiaoxi River Basin in upstream of Taihu Lake Watershed. Chin Geogr Sci. 17(4):349–356.
Wilby RL, Keenan R. 2012. Adapting to flood risk under climate change. Prog Phys Geogr. 36(3): 348–378.
Wu P, Christidis N, Stott P. 2013. Anthropogenic impact on Earth's hydrological cycle. Nature Clim Change. 3(9):807–810.
Zhai P, Pörtner HO, Roberts D, Skea J, Shukla PR, Pirani A, Connors S. 2018. Global warming of 1.5 OC: An IPCC special report on the impacts of global warming of 1.5° C above pre-industrial levels and related global greenhouse gas emission pathways, in the context of strengthening the global response to the threat of climate change, sustainable development, and efforts to eradicate poverty. (p. 32. V. Masson-Delmotte (ed.). Geneva, Switzerland: World Meteorological Organization.
Zope PE, Eldho TI, Jothiprakash V. 2016. Impacts of land use–land cover change and urbanization on flooding: A case study of Oshiwara River Basin in Mumbai, India. Catena. 145:142–154.